RSC Advances

COMMUNICATION

View Article Online
View Journal | View Issue

Cite this: *RSC Adv.*, 2015, **5**, 8340

Received 7th November 2014
Accepted 24th December 2014

DOI: 10.1039/c4ra14072a

www.rsc.org/advances

Extended isoindigo core: synthesis and applications as solution-processable n-OFET materials in ambient conditions†

Shiliang Xu,[ab] Na Ai,[c] Jie Zheng,[a] Na Zhao,[a] Zhenggang Lan,[a] Lirong Wen,[b] Xiao Wang,*[a] Jian Pei[c] and Xiaobo Wan*[a]

Two isoindigo derivatives fused with benzothiophene (**C20-DBTII**) and benzofuran (**C20-DBFII**) heterocycles have been synthesized. Solution-processed OFETs based on **C20-DBTII** showed ambient-stable ambipolar charge transport behaviour. OFETs based on the **C20-DBFII** show n-channel behaviour with electron mobility up to 0.074 $cm^2 V^{-1} s^{-1}$ in ambient conditions.

Organic semiconductors have received more and more attention as futuristic materials in recent years, and the past decades have seen the rapid development of organic semiconductors including organic field effect transistors (OFETs),[1] organic light-emitting diodes (OLEDs),[2] and organic photovoltaic cells (OPVCs).[3] These materials offer advantages of low-cost and flexible large-area electric circuits. The discovery of novel conjugated pigments boosts the growth in this area. Since two small molecules based on the isoindigo core were reported as electron donor materials for solar cells by Reynolds and co-workers in 2010,[4] more than 100 articles on various aspects have been published involving isoindigo-based materials.[5] Recently, isoindigo-based materials have received increasing attention for their promising performance in OFETs.[6] For instance, Pei and co-workers reported a fluorinated isoindigo-based conjugated polymer with a remarkable hole mobility of 3.62 $cm^2 V^{-1} s^{-1}$.[7] Recently, Kim *et al.* synthesized a thienoisoindigo-naphthalene polymer with an ultrahigh mobility of 14.4 $cm^2 V^{-1} s^{-1}$.[8]

Although tremendous achievements have been made on polymeric OFET materials containing isoindigo core,[9] the development of small molecular n-type or ambipolar OFET materials that could be operated in ambient conditions[10] is still an important task, since compared to polymers, small molecules have many advantages: (1) fixed molecular weight, identical structure and physical properties, no batch-to-batch variations,[11] (2) easy purification by chromatography, sublimation or recrystallization, (3) diverse fabrication methods of small molecular OFET devices, including high-vacuum deposition, spin-casting and single crystal growth. However, although oligomers based on isoindigo have been tested for OPVCs, the use of isoindigo for small molecular OFETs was less studied.[12] It was not until 2014 Yue *et al.* reported an OFET device based on a dicyanated isoindigo showing electron mobility up to 0.044 $cm^2 V^{-1} s^{-1}$.[12c] Marder and co-workers also synthesized a tetracyanated thienoisoindigo which shows good electron mobility with value up to 0.09 $cm^2 V^{-1} s^{-1}$ in inkjet-printed devices.[12d]

We are focused on the manipulation of the isoindigo core for better OFETs. Previously, our group synthesized thiophene-fused isoindigo (as shown in Scheme 1) and disclosed its photophysical and electrochemical properties, showing that the intramolecular charge transfer was enhanced.[13] In this communication, we further extended the conjugated system by fusing isoindigo with benzofuran or benzothiophene moiety, and investigated their OFET performance. Since isoindigo core is electron-deficient and benzothiophene or benzofuran terminal is electron-rich, it might form an intramolecular Donor–Acceptor–Donor (D–A–D) structure, which we speculated will lead to improved performance. Two solution-processable isoindigo derivatives (**C20-DBTII** and **C20-DBFII**) were thus synthesized. Both **C20-DBTII** and **C20-DBFII** exhibit relatively low-lying LUMO level, which facilitates electron transfer. **C20-DBTII** shows ambipolar charge transport behavior (0.011 $cm^2 V^{-1} s^{-1}$ for electrons and 5.72×10^{-4} $cm^2 V^{-1} s^{-1}$ for holes) and **C20-DBFII** exhibits good electron mobility up to 0.074 $cm^2 V^{-1} s^{-1}$ (as shown in Table 2) in ambient conditions.

[a]*Qingdao Institute of Bioenergy & Bioprocess Technology, Chinese Academy of Sciences, 189 Songling Road, Qingdao, Shandong Province, 266101, P. R. China. E-mail: wanxb@qibebt.ac.cn; Fax: +86-532-80662740; Tel: +86-532-80662740*

[b]*State Key Laboratory Base of Eco-Chemical Engineering, College of Chemistry and Molecular Engineering, Qingdao University of Science and Technology, Qingdao 266042, P. R. China*

[c]*College of Chemistry and Molecular Engineering, Peking University, Beijing 100871, P. R. China*

† Electronic supplementary information (ESI) available. See DOI: 10.1039/c4ra14072a

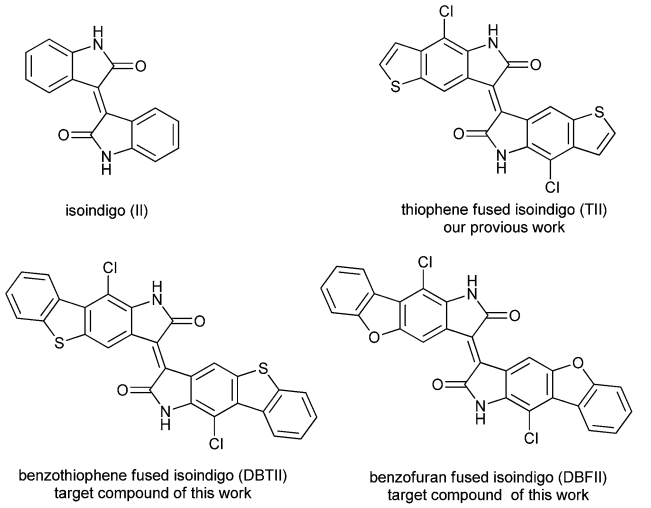

Scheme 1 The manipulation on the isoindigo core.

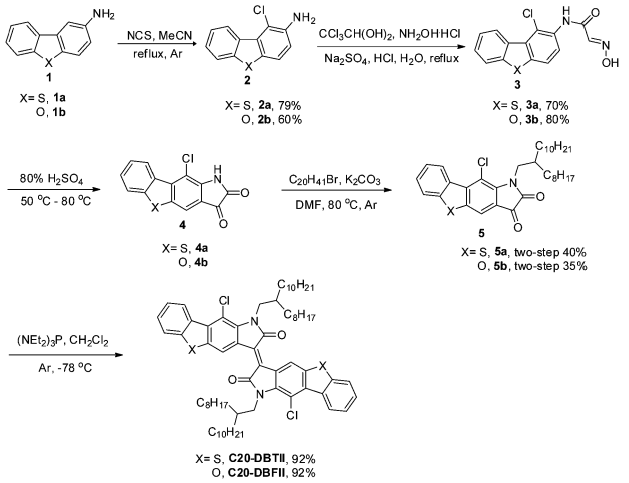

Scheme 2 The synthetic routes towards C20-DBTII and C20-DBFII.

The synthetic route toward both compounds is shown in Scheme 2. Briefly, chlorination at 1-position of commercially available 2-amino-dibenzo[*b*,*d*]thiophene **1a** afforded compound **2a** in good yield, which is a necessary step to force the subsequent Friedel–Crafts reaction to occur at 3-position of the dibenzothiophene core, as reported in our previous work.[13] Furthermore, since the introduction of chlorine atom to the isoindigo core has been proved to be effective to improve electron transport of conjugated polymers,[14] we anticipate similar effects might be observed on the extended isoindigo core. Treating **2a** with chloral hydrate and hydroxylamine hydrochloric acid afforded **3a** in 70% yield, which cyclized when treated with 80% H_2SO_4 to give the corresponding indole-2,3-dione **4a** as a crude product. The crude product was not purified due to its poor solubility but carried out directly to the next step for alkylation, and the product **5a** was then purified by chromatography. Upon treatment with $P(NEt_2)_3$, **5a** was converted to **C20-DBTII** in excellent yield. The overall yield for five steps is 20%. **C20-DBFII** was synthesized in the same manner with similar overall yield. Both **C20-DBTII** and **C20-DBFII** showed good solubility in common organic solvents, such as dichlorobenzene (10 mg mL^{-1}), thus makes them good candidates for solution processable OFETs.

The band gap and the HOMO–LUMO energy level are important parameters to determine the properties of organic semiconductors. UV-vis spectra of **C20-DBTII** and **C20-DBFII** in solution state and in film state are shown in Fig. 1 and S2, ESI† respectively. Both **C20-DBTII** and **C20-DBFII** exhibit relatively high and similar absorption coefficient in chloroform ($\varepsilon = 3.94 \times 10^4$ and 4.33×10^4 dm^3 mol^{-1} cm^{-1}, respectively). An intense absorption band (compared to that of isoindigo) with the peak at 501 nm and 485 nm was observed for **C20-DBTII** and **C20-DBFII** respectively (Fig. 1a). Interestingly, an absorption shoulder located around 600 nm was observed for **C20-DBFII**, which could not be seen for **C20-DBTII**. The calculated UV-vis spectra (shown in Fig. 1b) are in good agreement with the experimental results. The maximum absorption for both **C20-DBTII** and **C20-DBFII** is assigned to energy transition between HOMO−2 and LUMO. The absorption shoulder of **C20-DBFII** is assigned to its energy transition between HOMO and LUMO. On the other hand, the oscillation strength of HOMO–LUMO transition of **C20-DBTII** is very weak (located at 613 nm, OS: 0.03, Table S1 ESI†), indicating that this HOMO–LUMO transition could hardly be detected by UV-vis spectroscopy. This is due to the mismatch of the two orbitals in **C20-DBTII**. The orbital distribution along the two molecules is clearly shown in Fig. S3, ESI.† The LUMOs of both molecules are similar, in which the orbitals are mainly located the central core. This indicates that the dilactam core contributes most to LUMO. However, the HOMOs of the two species are quite different. The HOMO electron density of **C20-DBTII** at the central core is quite low, while a rather large density is observed at the same region for the HOMO of **C20-DBFII**. Therefore, the HOMO–LUMO of **C20-DBTII** overlap less than that of **C20-DBFII**, naturally leading to the rather small transition dipole moment between its HOMO and LUMO. In consequence, while the onset of the UV-vis absorption of **C20-DBFII** represents its HOMO–LUMO gap (1.79 eV), that of **C20-DBTII** mainly reflects its HOMO−2–LUMO gap (2.20 eV). The HOMO−2–LUMO band gap (2.27 eV) of **C20-DBFII** could be deduced from its major absorption peak, which is similar to that of **C20-DBTII**. Overall, the change in UV-vis spectra of the two molecules indicates that the replacement of S atom by O atom leads to an obvious change in the electronic structure in this conjugated system. In thin film state, both the UV-vis spectra of **C20-DBTII** and **C20-DBFII** showed an obvious hypsochromic shift (30 nm for **C20-DBTII** and 19 nm for **C20-DBFII**, Fig. S2, ESI†), suggesting that both molecules might take same molecular stacking mode (H-aggregate) in solid state, due to their similar structure.

LUMO energy level of the two compounds was determined by cyclic voltammetry, as shown in Fig. S4, ESI.†[15] Despite the difference in the structure, both **C20-DBTII** and **C20-DBFII** exhibit two pairs of quasi-reversible redox waves, with the similar half-wave reductive potential, indicating that the

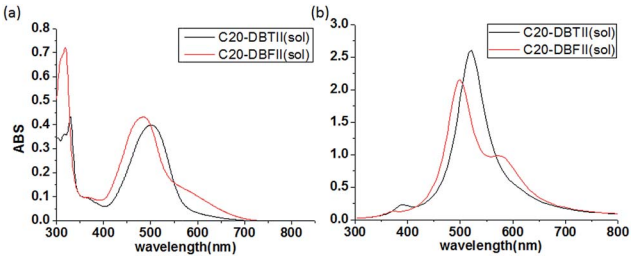

Fig. 1 (a) Normalized UV-vis absorption of 10^{-5} mol L^{-1} **C20-DBTII** and **C20-DBFII** in chloroform; (b) calculated UV-vis absorption of **C20-DBTII** and **C20-DBFII** in chloroform (DFT(B3LYP/6-31+G*)).

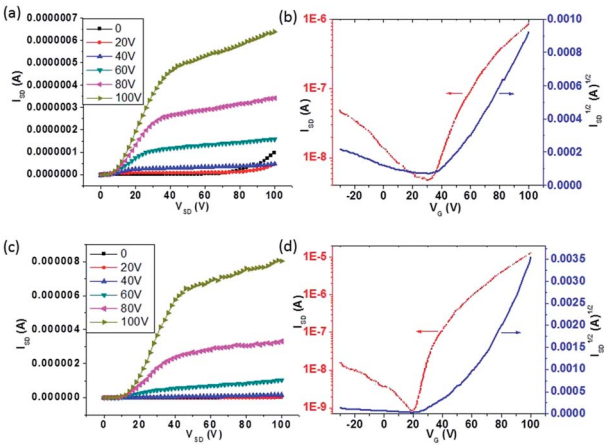

Fig. 2 (a) Output characteristics and (b) transfer characteristics of **C20-DBTII** OFET devices; (c) output characteristics and (d) transfer characteristics of **C20-DBFII** OFET devices; output characteristics at n-channel operation and transfer characteristics at electron-enhancement operation; device dimensions ratio of channel width to channel length = 20; all devices are measured in ambient conditions.

electron-injection ability was mainly determined by the isoindigo core. The energy level of LUMO of these isoindigo derivatives were calculated using $E_{LUMO} = -e(E_{1/2}{}^{0/-} + 4.44)$ eV equation (referring to Ag/AgCl electrode), as shown in Table 1. The $E_{1/2}{}^{0/-}$ of **C20-DBTII** and **C20-DBFII** is −0.72 eV and −0.71 eV, which corresponds to E_{LUMO} at −3.72 eV and −3.73 eV respectively. The HOMO energy level (E_{HOMO}) of **C20-DBFII** is −5.52 eV, deduced from the equation $E_{HOMO} = E_{LUMO} - E_g^{opt}$. The HOMO−2 energy level (E_{HOMO-2}) of **C20-DBTII** and **C20-DBFII** can also be estimated using the similar equation $E_{HOMO-2} = E_{LUMO} - E_{g-2}^{opt}$, which is −5.92 eV and −6.00 eV respectively.

In order to evaluate the performance of the electronic devices of **C20-DBTII** and **C20-DBFII**, two top-gate/bottom-contact organic thin-film transistors were fabricated with a SiO_2/Si substrates and Au source/drain electrodes (Fig. S5, ESI†). The thin films were spin-coated onto SiO_2/Si substrates using a dichlorobenzene (DCB) solution containing **C20-DBTII** or **C20-DBFII** (10 mg mL^{-1}) in a nitrogen-filled glovebox. A CYTOP solution was spin-coated on the top of the semiconducting layer and cross-linked at 100 °C for 1 h as the dielectric layer. Then, an aluminium layer was thermally evaporated as the gate electrode. The device performance was investigated in ambient conditions (Fig. 2 and S6, ESI†) and the results were summarized in Table 2. OFETs based on **C20-DBTII** show ambipolar charge transport behaviour. The electron mobility is up to 0.011 $cm^2\ V^{-1}\ s^{-1}$, with a threshold voltage of 47 V. The hole mobility is up to 5.72×10^{-4} $cm^2\ V^{-1}\ s^{-1}$, with a threshold voltage of −53 V. On the other hand, OFETs based on **C20-DBFII** show only n-channel charge transport behaviour, with electron mobility up to 0.074 $cm^2\ V^{-1}\ s^{-1}$, with the threshold voltage value of 40 V. It is worthwhile to mention that **C20-DBTII** and **C20-DBFII** decomposed at 356 °C and 348 °C respectively, showing their excellent thermal stability (TGA trace, shown in Fig. S1, ESI†).

The device test results indicate that both molecules are good n-type semiconductors (**C20-DBTII** is better), but not good p-type semiconductors: the hole mobility of **C20-DBTII** is twenty times smaller than its electron mobility, and the hole mobility of **C20-DBFII** could not be detected. Although according to the calculated results, **C20-DBTII** and **C20-DBFII** should have similar HOMO–LUMO energy level thus should show similar charge transport behaviour, there might be some other reasons to explain why DBFII does not exhibit p-type character. One possible reason is that O atom is more electronegative than S atom, while S atom is easier to be polarized since it is larger in size than O atom. Overall, the removal of an electron from **C20-DBTII** is easier than from **C20-DBFII**.

As to their n-type OFET performance, **C20-DBFII** showed better electron mobility and smaller threshold voltage than **C20-DBTII**. We reasoned that the difference in the OFET performance of the two molecules might be due to their different crystallinity and morphology. The crystallinity and molecular orientations of thin films were then investigated by X-ray diffraction (XRD) analysis. The out of plane XRD patterns of the thin films of **C20-DBTII** and **C20-DBFII** are shown in Fig. 3. **C20-DBFII** shows sharp and intense peaks, but **C20-DBTII** shows weak peaks, indicating the better crystallinity of **C20-DBFII** film. The *d*-spacing of both molecules were calculated from the out-of-plane XRD patterns and Bragg equation. **C20-DBTII** and **C20-DBFII** films exhibited primary diffraction peaks at 2θ of 4.28° and 4.13°, corresponding to *d*(100)-spacing

Table 1 UV-vis absorption and electrochemical properties of **C20-DBTII** and **C20-DBFII**

Compounds	λ_{max}^{sol} (nm)	λ_{max}^{film} (nm)	$E_{1/2}{}^{0/-}$ (V)	$E_{1/2}{}^{-/2-}$ (V)	E_{LUMO} (eV)	E_{HOMO} (eV)	E_{HOMO-2} (eV)
C20-DBTII	501	471	−0.72	−1.11	−3.72	—	−5.92
C20-DBFII	485	466	−0.71	−1.12	−3.73	−5.52	−6.00

Table 2 OFET performance of **C20-DBTII** and **C20-DBFII** thin films under ambient

Compounds	μ_e ($cm^2\ V^{-1}\ s^{-1}$)	V_T (V)	I_{on}/I_{off}	μ_h ($cm^2\ V^{-1}\ s^{-1}$)	V_T (V)	I_{on}/I_{off}
C20-DBTII	0.011	47	1.8×10^2	5.72×10^{-4}	−53	2.5×10^2
C20-DBFII	0.074	40	1.5×10^4	N.A.		

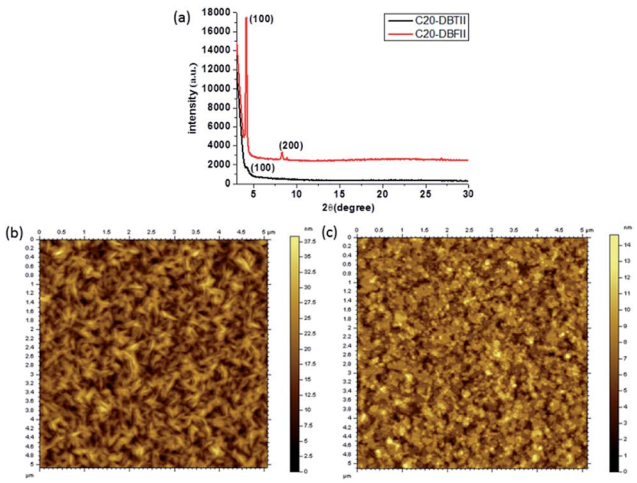

Fig. 3 (a) Out-of-plane X-ray diffraction (XRD) patterns of **C20-DBTII** and **C20-DBFII** thin films; (b) AFM height images (5 × 5 μm^2) of **C20-DBTII** thin films; (c) AFM height images (5 × 5 μm^2) of **C20-DBFII** thin films; thin films were spin-coated onto SiO_2/Si substrates from DCB solutions (10 mg mL^{-1}).

of 20.65 and 21.37 Å, respectively. The *d*(100)-spacing of **C20-DBTII** and **C20-DBFII** are a little bit longer than the theoretically calculated molecular lengths (**C20-DBTII**, molecular length ∼ 19.94 Å; **C20-DBFII**, molecular length ∼ 19.45 Å), suggesting a vertical alignment of molecular configuration on the substrate surface. **C20-DBFII** also showed a diffraction peak at 2θ of 8.28°, which is assigned to (200) diffraction, with *d*(200)-spacing of 10.67 Å. Clearly, **C20-DBFII** shows stronger *d*-spacing signal, indicating a better layer-by-layer packed lamellar structure, which accounts for better electron mobility of **C20-DBFII** than **C20-DBTII**.

Besides crystallinity, the semiconductor film morphology is another decisive factor that affects charge transport properties. The morphology of the as-grown **C20-DBTII** and **C20-DBFII** films for OFET study was investigated using atomic force microscopy (AFM), and the results are shown in Fig. 3. AFM height images showed that both films formed densely packed nanofibrillar network with relatively smooth surface roughness. However, although **C20-DBTII** films exhibited larger fibrillar aggregates (RMS ∼ 5.04 nm) than **C20-DBFII** (RMS ∼ 1.71 nm), they also showed more obvious grain boundaries than **C20-DBFII**. Larger boundaries are deleterious to the charge transport, which explains why the electron mobility of **C20-DBTII** film is almost seven times smaller than that of **C20-DBFII** film.

Conclusions

Two isoindigo derivatives fused with benzothiophene and benzofuran heterocycles (**C20-DBTII** and **C20-DBFII**) have been synthesized and characterized. Solution-processed OFETs based on these two molecules exhibited stable performance in ambient conditions due to their low-lying LUMO level. **C20-DBTII** showed ambipolar charge transport behaviour while **C20-DBFII** showed n-channel behaviour with electron mobility up to 0.074 $cm^2\ V^{-1}\ s^{-1}$ in ambient conditions. This is the first example using fused isoindigo small molecules for OFET applications, indicating the potential applications of isoindigo derivatives not only in polymeric system, but also in small molecular system for organic semiconductors.

Acknowledgements

This work is supported by "100 Talents" Program from Chinese Academy of Sciences and National Science Foundation of China (NSFC no. Y406371106, 21174157, 21103213, 91233106).

Notes and references

1 (*a*) C. Wang, H. Dong, W. Hu, Y. Liu and D. Zhu, *Chem. Rev.*, 2012, **112**, 2208–2267; (*b*) C. A. Di, F. Zhang and D. Zhu, *Adv. Mater.*, 2013, **25**, 313–330.
2 A. C. Grimsdale, K. Leok Chan, R. E. Martin, P. G. Jokisz and A. B. Holmes, *Chem. Rev.*, 2009, **109**, 897–1091.
3 (*a*) Y. Huang, E. J. Kramer, A. J. Heeger and G. C. Bazan, *Chem. Rev.*, 2014, **114**, 7006–7043; (*b*) J. Roncali, P. Leriche and P. Blanchard, *Adv. Mater.*, 2014, **26**, 3821–3838.
4 J. Mei, K. R. Graham, R. Stalder and J. R. Reynolds, *Org. Lett.*, 2010, **12**, 660–663.
5 (*a*) B. Liu, Y. Zou, B. Peng, B. Zhao, K. Huang, Y. He and C. Pan, *Polym. Chem.*, 2011, **2**, 1156–1162; (*b*) Z. Ma, E. Wang, M. E. Jarvid, P. Henriksson, O. Inganas, F. Zhang and M. R. Andersson, *J. Mater. Chem.*, 2012, **22**, 2306–2314.
6 (*a*) T. Lei, J. Y. Wang and J. Pei, *Acc. Chem. Res.*, 2014, **47**, 1117–1126; (*b*) E. Wang, W. Mammo and M. R. Andersson, *Adv. Mater.*, 2014, **26**, 1801–1826.
7 T. Lei, J. H. Dou and J. Pei, *Adv. Mater.*, 2012, **24**, 6457–6461.
8 G. Kim, S. J. Kang, G. K. Dutta, Y. K. Han, T. J. Shin, Y. Y. Noh and C. Yang, *J. Am. Chem. Soc.*, 2014, **136**, 9477–9483.
9 (*a*) G. Zhang, Y. Fu, Z. Xie and Q. Zhang, *Macromolecules*, 2011, **44**, 1414–1420; (*b*) T. Lei, J. H. Dou, Z. J. Ma, C. H. Yao, C. J. Liu, J. Y. Wang and J. Pei, *J. Am. Chem. Soc.*, 2012, **134**, 20025–20028; (*c*) Y. Yang, R. Wu, X. Wang, X. Xu, Z. Li, K. Li and Q. Peng, *Chem. Commun.*, 2014, **50**,

439–441; (*d*) T. Lei, Y. Cao, X. Zhou, Y. Peng, J. Bian and J. Pei, *Chem. Mater.*, 2012, **24**, 1762–1770.

10 (*a*) Y. Takeda, T. L. Andrew, J. M. Lobez, A. J. Mork and T. M. Swager, *Angew. Chem., Int. Ed.*, 2012, **51**, 9042–9046; (*b*) H. Li, F. S. Kim, G. Ren and S. A. Jenekhe, *J. Am. Chem. Soc.*, 2013, **135**, 14920–14923; (*c*) T. Lei, X. Xia, J. Y. Wang, C. J. Liu and J. Pei, *J. Am. Chem. Soc.*, 2014, **136**, 2135–2141.

11 J. Zhang, G. Wu, C. He, D. Deng and Y. Li, *J. Mater. Chem.*, 2011, **21**, 3768–3774.

12 (*a*) T. Wu, C. Yu, Y. Guo, H. Liu, G. Yu, Y. Fang and Y. Liu, *J. Phys. Chem. C*, 2012, **116**, 22655–22662; (*b*) S. S. Dharmapurikar, A. Arulkashmir, C. Das, P. Muddellu and K. Krishnamoorthy, *ACS Appl. Mater. Interfaces*, 2013, **5**, 7086–7093; (*c*) W. Yue, T. He, M. Stolte, M. Gsanger and F. Wurthner, *Chem. Commun.*, 2014, **50**, 545–547; (*d*) R. R. Dasari, A. Dindar, C. K. Lo, C.-Y. Wang, C. Quinton, S. Singh, S. Barlow, C. Fuentes-Hernandez, J. R. Reynolds, B. Kippelen and S. R. Marder, *Phys. Chem. Chem. Phys.*, 2014, **16**, 19345–19350.

13 N. Zhao, L. Qiu, X. Wang, Z. An and X. Wan, *Tetrahedron Lett.*, 2014, **55**, 1040–1044.

14 T. Lei, J.-H. Dou, Z.-J. Ma, C.-J. Liu, J.-Y. Wang and J. Pei, *Chem. Sci.*, 2013, **4**, 2447–2452.

15 C. M. Cardona, W. Li, A. E. Kaifer, D. Stockdale and G. C. Bazan, *Adv. Mater.*, 2011, **23**, 2367–2371.

